

***Magnetic fields in barred galaxies V. Modelling
NGC 1365***

Moss, D and Snodin, A. P. and Englmaier,
P and Shukurov, A and Beck, R and V, D. D.

2007

MIMS EPrint: **2008.94**

Manchester Institute for Mathematical Sciences
School of Mathematics

The University of Manchester

Reports available from: <http://eprints.maths.manchester.ac.uk/>

And by contacting: The MIMS Secretary
School of Mathematics
The University of Manchester
Manchester, M13 9PL, UK

ISSN 1749-9097

Magnetic fields in barred galaxies

V. Modelling NGC 1365

D. Moss¹, A. P. Snodin², P. Englmaier³, A. Shukurov², R. Beck⁴, and D. D. Sokoloff⁵

¹ School of Mathematics, University of Manchester, Oxford Road, Manchester, M13 9PL, UK

² School of Mathematics and Statistics, University of Newcastle, Newcastle upon Tyne, NE1 7RU, UK
e-mail: andrew.snodin@ncl.ac.uk

³ Institute of Theoretical Physics, University of Zürich, Winterthurerstrasse 190, 8057 Zürich, Switzerland

⁴ Max-Planck-Institut für Radioastronomie, Auf dem Hügel 69, 53121 Bonn, Germany

⁵ Department of Physics, Moscow State University, 119992 Moscow, Russia

Received 9 August 2006 / Accepted 3 January 2007

ABSTRACT

Aims. We present a model of the global magnetic field in the barred galaxy NGC 1365 based jointly on the large-scale velocity field of interstellar gas fitted to HI and CO observations of this galaxy and on mean-field dynamo theory. The aim of the paper is to present a detailed quantitative comparison of a galactic dynamo model with independent radio observations.

Methods. We consider several gas dynamical models, based on two rotation curves. We test a range of nonlinear dynamo models that include plausible variations of those parameters that are poorly known from observations. Models for the cosmic ray distribution in the galaxy are introduced in order to produce synthetic radio polarization maps that allow direct comparison with those observed at $\lambda\lambda 3.5$ and 6.2 cm.

Results. We show that the dynamo model is robust in that the most important magnetic features are controlled by the relatively well established properties of the density distribution and gas velocity field. The optimal agreement between the synthetic polarization maps and observations is obtained when a uniform cosmic ray distribution is adopted. These maps are sensitive to the number density of thermal ionized gas because of Faraday depolarization effects. Our results are compatible with the observed polarized radio intensity and Faraday rotation measure if the degree of ionization is between 0.01 and 0.2 (with respect to the total gas density, rather than to the diffuse gas alone). We find some indirect evidence for enhanced turbulence in the regions of strong velocity shear (spiral arms and large-scale shocks in the bar) and within 1–2 kpc of the galactic centre. We confirm that magnetic stresses can drive an inflow of gas into the inner 1 kpc of the galaxy at a rate of a few $M_{\odot} \text{ yr}^{-1}$.

Conclusions. The dynamo models are successful to some extent in modelling the large scale regular magnetic field in this galaxy. Our results demonstrate that dynamo models and synthetic polarization maps can provide information about both the gas dynamical models and conditions in the interstellar medium. In particular, it seems that large-scale deviations from energy equipartition (or pressure balance) between large-scale magnetic fields and cosmic rays are unavoidable. We demonstrate that the dynamical effects of magnetic fields cannot be everywhere ignored in galaxy modelling.

Key words. galaxies: magnetic fields – galaxies: individual: NGC1365 – galaxies: spiral – ISM: magnetic fields

1. Introduction

NGC 1365 is one of the best studied barred galaxies. It has been observed in a broad range of wavelengths, including HI (Ondrechen & van der Hulst 1989), molecular gas (Curran et al. 2001), H α (Lindblad 1999), and the radio range (Sanqvist et al. 1995; Beck et al. 2005), in addition to numerous optical and infrared observations (see Lindblad 1999, and references therein). Detailed gas dynamical modelling by Lindblad et al. (1996) provided quantitative models for the gravity and gas velocity fields in this galaxy that fit the HI and, to some extent, the CO observations.

The aim of this paper is to add to these efforts by the inclusion of magnetic fields. The gas dynamical and magnetic field model of the galaxy can then be tested against independent radio data, which were not included in the construction of the model. Of course, this involves an additional piece of theory and some further assumptions (concerning, e.g., the applicability of dynamo theory to galaxies and uncertainties in some dynamo parameters). Some features of the dynamo theory certainly

are not understood well enough. However, we demonstrate that gross features of the model galactic magnetic field – at least in barred galaxies where the shear in the large-scale velocity is the dominant induction effect – are rather insensitive to the poorly known details of the dynamo system (most importantly, the α -coefficient). Therefore, we can plausibly constrain the freedom within the dynamo models, and so draw conclusions about the interstellar medium in barred galaxies.

We find fair agreement between radio polarization observations and the magnetic field obtained as a solution of the mean-field dynamo equations, using velocity and density fields obtained from gas dynamical simulations, although the distribution of polarized intensity is reproduced better than that of polarization angles. Our models also support the idea that interstellar turbulence is enhanced in the vicinity of dust lanes near the bar major axis, and that the energy density of cosmic rays can depend only weakly on position in the galaxy, thus deviating significantly from equipartition with interstellar magnetic field. As a result, radio polarization observations and modelling of

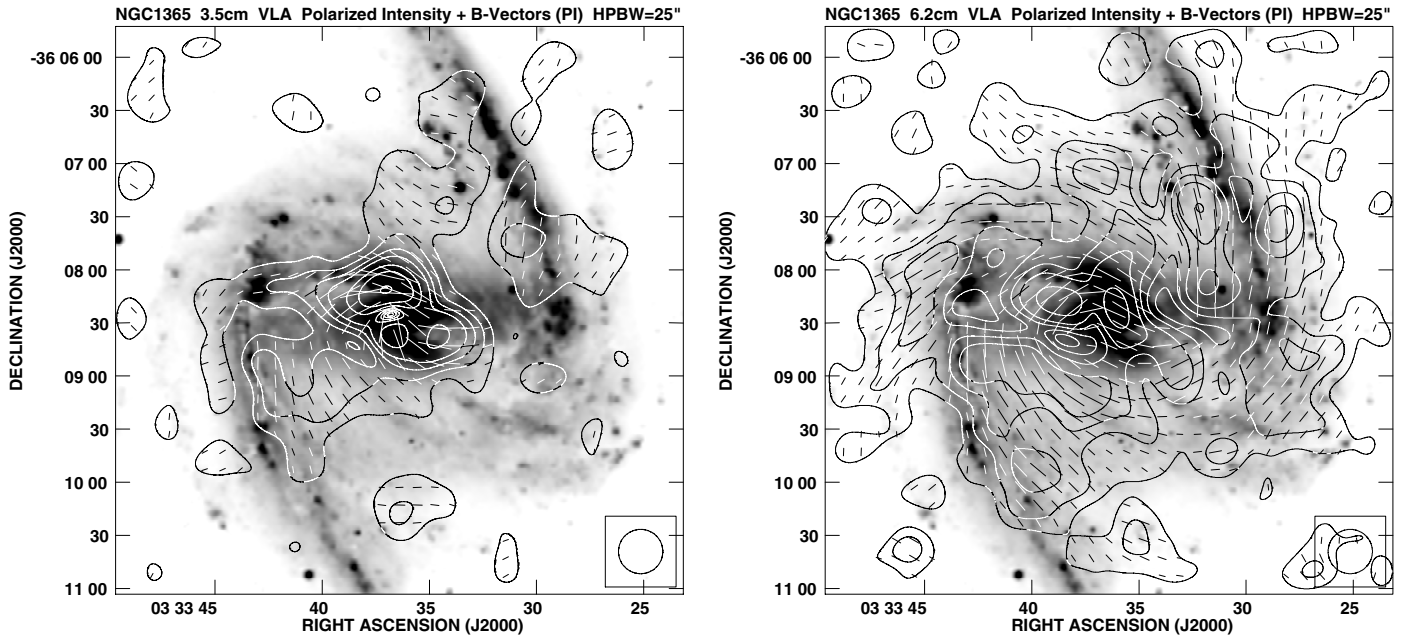


Fig. 1. The polarized intensity contours and magnetic vectors of the polarized radio emission at the wavelengths $\lambda 3.5$ cm (left hand panel) and $\lambda 6.2$ cm (right hand panel) (both smoothed to a resolution $25''$; the beam size is shown in the lower right of each panel), superimposed onto an ESO optical image of NGC 1365, kindly provided by P. O. Lindblad. The contour levels are 1, 2, 3, 4, 6, 8, 12, ... times $30 \mu\text{Jy}/\text{beam}$ at $\lambda 3.5$ cm and $40 \mu\text{Jy}/\text{beam}$ at $\lambda 6.2$ cm; the rms noise is $15 \mu\text{Jy}/\text{beam}$ at $\lambda 3.5$ cm and $14 \mu\text{Jy}/\text{beam}$ at $\lambda 6.2$ cm.

magnetic fields are important ingredients of both the theory and observations of barred galaxies. This work resembles quite strongly an earlier study of another barred galaxy, NGC 1097 (Moss et al. 2001), but represents a significant improvement in that we now use a dynamical model that specifically models NGC 1365, rather than the generic dynamical model adopted for NGC 1097. Also, the dynamo model we use here is fully three dimensional, whereas that of Moss et al. (2001) used the “no- z ” approximation to remove explicit dependence on the vertical coordinate. Broadly comparable studies have also been published by Otmianowska-Mazur et al. (2002), Soida et al. (2006) and Vollmer et al. (2006).

2. The observed magnetic structure

NGC 1365 was observed in total and polarized radio continuum with the VLA DnC array at $\lambda 3.5$ cm and $\lambda 6.2$ cm. The full details and the maps at $15''$ and $25''$ angular resolution are given in Beck et al. (2005). The total radio intensity (a measure of total magnetic field strength and thermal emission) follows well the optical bar and the spiral arms. According to the observed spectral indices, the thermal fraction is about 20% at $\lambda 6.2$ cm.

The polarized emission (Fig. 1) is strongest in the central region and inner bar, but decreases rapidly towards the outer bar. There is also significant polarized emission between the bar and the spiral arms. No concentration in the spiral arms can be detected. At $\lambda 6.2$ cm, where the sensitivity is highest, the polarized emission forms a smooth halo around the bar. The degree of polarization is low in the bar and spiral arms, indicating that the turbulent magnetic field dominates in the regions of high gas density and strong star formation, while the regular field is strong between the bar and the spiral arms. At $\lambda 3.5$ cm, most of the extended polarized emission outside the bar is lost in the noise because of the steep synchrotron spectrum. Furthermore, the sensitivity of the VLA to extended structures is reduced for

scales beyond 3 arcmin at $\lambda 3.5$ cm, which affects the visibility of the large-scale polarized emission in NGC 1365, while at $\lambda 6.2$ cm the critical limit is 5 arcmin and so does not affect our observations.

The peak polarized intensity is 368 mJy per beam at $\lambda 3.5$ cm in the massive dust lane northeast of the centre (see Beck et al. 2005). The fractional polarization is 0.8. At the same position the $\lambda 6.2$ cm map reveals a local *minimum* with polarized intensity of 150 mJy/beam, corresponding to a fractional polarization of only 0.2, which is near the expected contribution from instrumental polarization by the bright nuclear region. This indicates that strong depolarization occurs at $\lambda 6.2$ cm in the central region, by a factor of at least 4. In the bar and spiral arms the depolarization factor is 2–3 (Beck et al. 2005).

Polarized emission can emerge from coherent, regular magnetic fields or from anisotropic random magnetic fields; these possibilities can be distinguished with the help of Faraday rotation measures. In NGC 1097, anisotropic fields dominate in the bar region (Beck et al. 2005). However, due to the weak polarized intensity in NGC 1365, the observations available cannot provide a large-scale map of Faraday rotation, so that the relative contributions of coherent and anisotropic random magnetic fields remains unclear.

3. The model

3.1. Gas dynamical models of NGC 1365

We reproduced the gas dynamical model of Lindblad, Lindblad & Athanassoula (1996) using their gravitational potential “BSM” kindly provided to us by P. O. Lindblad. This potential (the “LLA model” in the following) includes the gravitational potentials of the disc and spiral arms and was derived from the nonaxisymmetric part of the deprojected J -band image. Their best fit parameters are $A_{\text{bar}} = 1.2$ and $A_{\text{spiral}} = 0.3$ for the relative contributions of the bar and spiral arms. The model

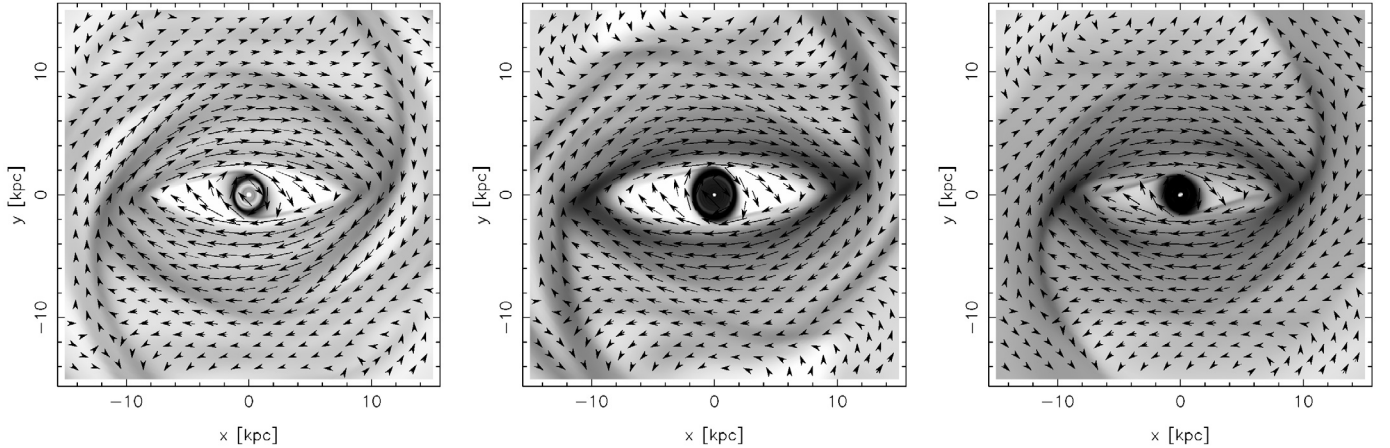


Fig. 2. The model gas density with superimposed velocity vectors in the reference frame corotating with the bar, in gas dynamical models based on (a) the rotation curve of the LLA model with $c_s = 10 \text{ km s}^{-1}$ (left hand panel), and the rotation curve of Sofue et al. (1999) with (b) $c_s = 10 \text{ km s}^{-1}$ (middle panel) and (c) $c_s = 30 \text{ km s}^{-1}$ (right hand panel), with c_s the sound speed. Shades of grey represent the logarithm of gas density (darker shades corresponding to larger values), with each shade corresponding to the same density in each panel. Note the smaller density contrast in the bar region in the model with higher speed of sound (panel c).

rotation curve fits the HI rotation curve for galactocentric distances $r > 120''$ and gives reasonable resonance locations inside this radius. Various versions of the LLA model used the bar angular velocity of $\Omega_p = 18 \text{ km s}^{-1} \text{ kpc}^{-1}$ (model BSM) and $17 \text{ km s}^{-1} \text{ kpc}^{-1}$ (model BSM2), with the corotation radius close to 14 kpc in both cases.

The full gravitational potential of the LLA model is obtained from two independent observations: (i) the HI rotation curve, used to fix the total radial mass distribution of the galaxy including dark matter; and (ii) the *J*-band data, tracing the stellar mass distribution, which is only used to derive (after deprojection) the amplitude of nonaxisymmetric perturbations in the disc plane. The latter cannot be used to derive the rotation curve reliably because of the presence of dark matter, and the former also can be misleading when the gas flow is significantly nonaxisymmetric.

Lindblad et al. (1996) adopted 20 Mpc ($1'' = 97 \text{ pc}$) for the distance of NGC 1365, but we adjusted the model to a distance of 18.6 Mpc ($1'' = 90 \text{ pc}$) (Lindblad 1999).

Isothermal gas dynamical models were calculated using the code ZEUS 2D, published by Stone & Norman (1992), and we found a close match to the model of Lindblad et al. (1996). However we did not attempt to take into account the warp in the outer disc, as we are mostly interested in the inner region. Our basic models, illustrated in Fig. 2b,c have the bar angular velocity $\Omega_p = 16.16 \text{ km s}^{-1} \text{ kpc}^{-1}$ and the corotation radius at $R_c = 15.5 \text{ kpc}$; we also considered a model (Fig. 2a) with $\Omega_p = 17 \text{ km s}^{-1} \text{ kpc}^{-1}$ and $R_c = 16.3 \text{ kpc}$. The angular velocity of the spiral pattern is taken to be equal to that of the bar. For reasons explained below in Sect. 4, the resulting gas density in the bar region was too low to reproduce the observed magnetic field within the dynamo model. The gas density in the LLA model can be argued to be underestimated inside the corotation radius because the rotation curve used had poor resolution, and underestimates the depth of the potential well. We derived our basic model from the LLA model, by replacing the rotation curve used by Lindblad et al. (1996) with the more recent CO rotation curve of Sofue et al. (1999). This modified model was much better able to reproduce the observed magnetic field, while remaining in agreement with the overall morphology of the molecular gas distribution. A significant difference is that there is more material in the central regions when Sofue’s rotation curve is used.

The rotation curve used here is shown in Fig. 3a, with the positions of resonances illustrated in Fig. 3b.

We also studied the dependence of the gas dynamics and magnetic field on the sound speed adopted in the isothermal gas model. This parameter is uncertain in our models for several reasons. Englmaier & Gerhard (1997) showed that the large-scale gas distribution in isothermal gas flow models of barred galaxies can depend on the sound speed, even if the pressure forces are negligible. Since the position, and even existence, of shocks depends on Mach number, the global gas flow configuration can change as a result of a relatively small change in the speed of sound. Different parts of the multi-phase interstellar medium (ISM) may not follow the same global gas flow. Different numerical methods have been shown to represent different aspects of the ISM with varying success. Sticky particle methods, for example, model better the clumpy ISM, while grid-based methods give a better description of the shocks and the smooth gas component.

The global magnetic field depends on the gas flow via Eqs. (1) and (2); however, it is not a priori clear which component of the ISM carries the magnetic field and, therefore, what is the appropriate sound speed of the gas. We have considered models with the speed of sound equal to 10 and 30 km s^{-1} (see Sect. 5.4).

Our magnetic field model also relies on the gas density obtained from gas dynamical simulations together with the velocity field; this is discussed in Sect. 3.2 – see Eq. (4).

3.2. The dynamo model

Dynamo models, specifically simple mean-field turbulent dynamos, are remarkably successful in explaining the observed features of galactic magnetic fields (see, e.g., Ruzmaikin et al. 1988; Beck et al. 1996; Widrow 2002, for reviews). Despite the fact that the nonlinear behaviour of turbulent dynamos is still controversial, mean-field models provide a remarkably reliable empirical description of large-scale (regular) galactic magnetic fields (Shukurov 2004). Fortunately, dynamo solutions for galaxies are quite insensitive to those parameters that are poorly known, such as the form of the α -effect and even, to a lesser extent, the turbulent magnetic diffusivity. This is especially true

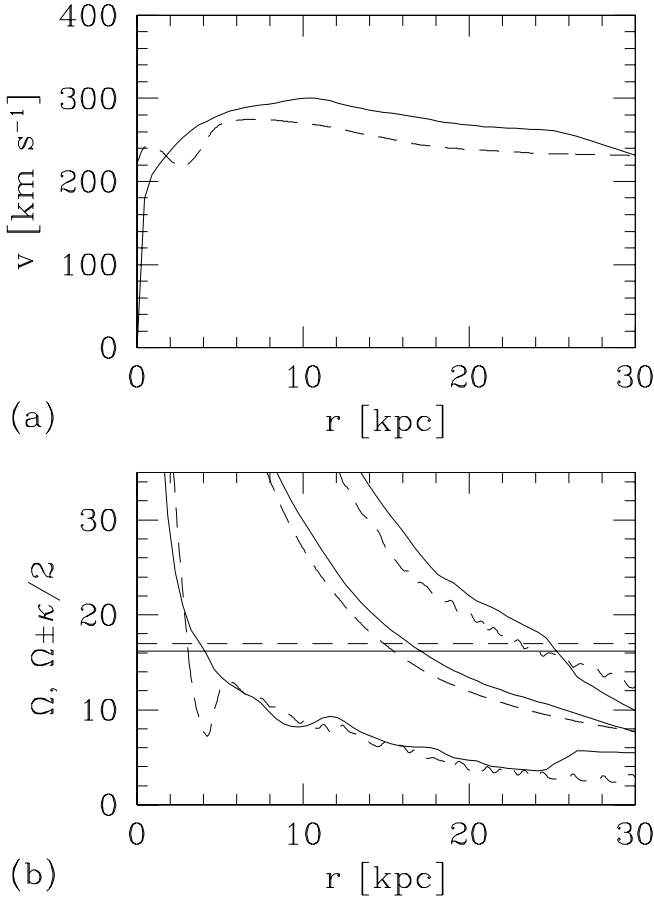


Fig. 3. a): The rotation curves used in the paper: that from Lindblad et al. (1996) (solid; as in Fig. 2a), and one more consistent with more recent CO observations (Sofue et al. 1999) (dashed; as in Fig. 2b,c). The plot assumes the distance of NGC 1365 to be 20 Mpc as in Lindblad et al. (1996). The radius of corotation is $R_c \approx 14$ kpc. **b):** The linear resonance diagram for the rotation curves shown in (a) with the same line style. From bottom to top: $\Omega - \kappa/2$, Ω , and $\Omega + \kappa/2$ in units of $\text{km s}^{-1} \text{kpc}^{-1}$. The resonances are located at the intersections with the horizontal lines corresponding to $\Omega_p = 16.16 \text{ km s}^{-1} \text{kpc}^{-1}$ (solid) and $17 \text{ km s}^{-1} \text{kpc}^{-1}$ (dashed). The small scale structure in the $\Omega \pm \kappa/2$ curves is an artefact of plotting.

of models for barred galaxies where large-scale velocity shear plays a dominant role in determining magnetic field structure (Moss et al. 1998a, 2001); then the primary role of the α -effect is to maintain the field against decay.

Our model can be regarded as a development of the dynamo model of Moss et al. (2001), used to model the large-scale magnetic field in a generic barred galaxy. We now introduce further elaborations required to reproduce the basic features of the global magnetic pattern in NGC 1365. We solve the standard mean field dynamo equation for the large-scale, regular magnetic field \mathbf{B}

$$\frac{\partial \mathbf{B}}{\partial t} = \nabla \times (\mathbf{u} \times \mathbf{B} + \alpha \mathbf{B} - \frac{1}{2} \nabla \eta \times \mathbf{B} - \eta \nabla \times \mathbf{B}), \quad (1)$$

in three spatial dimensions, using Cartesian coordinates (x, y, z) , where x and y are horizontal dimensions, and the disc midplane is at $z = 0$. Here α and η are the turbulent transport coefficients responsible for the α -effect and turbulent magnetic diffusion, respectively, \mathbf{u} is the large-scale velocity field, and the term with $\nabla \eta$ allows for the turbulent diamagnetism associated

with the spatial variation of the turbulent diffusivity (Roberts & Soward 1975). In our standard case, our computational domain covers the region $-L \leq (x, y) \leq L$, $0 \leq z \leq aL = z_{\text{max}}$, where a is the domain's aspect ratio. We take a mesh of size $n_x \times n_y \times n_z$, with uniform spacing in the horizontal directions and also, separately, vertically. The maximum resolution readily available to us was $n_x = n_y = 200$, $n_z = 31$, and in order to resolve satisfactorily the solutions we took $L = 15$ kpc and $a = 0.12$, so $z_{\text{max}} = 1.8$ kpc. (Thus we study only the inner part of this unusually large barred galaxy.) The total thickness of the gas layer that hosts the large-scale magnetic field is taken as $2h = 0.9$ kpc, compatible with the thickness of the diffuse warm gas in the Milky Way. Our procedure is to time-step the x and y components of Eq. (1), and then to use the condition $\nabla \cdot \mathbf{B} = 0$ to update B_z . We restrict ourselves to solutions of even (quadrupolar) parity with respect to the disc plane $z = 0$, and so the latter step is straightforward, given that $B_z = 0$ at $z = 0$. This is the same procedure used in the three-dimensional galactic dynamo models described in Moss (1997), except that cylindrical polar coordinates were used there.

In Eq. (1), α parameterizes the dynamo action of the interstellar turbulence, and η is the turbulent magnetic diffusivity. We assume both of these quantities to be scalars (rather than tensors) and, in order to obtain a steady state with saturated dynamo action, introduce a simple α -quenching nonlinearity into the problem, writing

$$\alpha = \frac{\alpha_0}{1 + \xi \mathbf{B}^2 / B_{\text{eq}}^2}, \quad B_{\text{eq}}^2 = 4\pi\rho(r)v_t^2, \quad (2)$$

$$\alpha_0 = \alpha_* \frac{\Omega(r)}{\Omega_0} f(z), \quad (3)$$

with

$$f(z) = \begin{cases} \sin(\pi z/h), & |z| \leq h/2, \\ \left[\cosh(2|z|/h - 1) \right]^{-1} \text{sgn } z, & |z| > h/2. \end{cases}$$

Here Ω_0 is a typical value of Ω , B_{eq} is the magnetic field strength corresponding to equipartition between magnetic and turbulent kinetic energies, and α_* is a constant, which we can adjust. Quite arbitrarily, we adopt $\Omega_0 = \Omega$ at $r = 3$ kpc, and Eq. (3) shows that α_* is the maximum value of α at this radius. Thus we are assuming that the large-scale magnetic field significantly reduces the α -effect when its energy density approaches that of the turbulence; the constant ξ is introduced to suggest formally some of the uncertainty about the details of this feedback. The dependence of α on height, defined by $f(z)$, is implicitly odd with respect to the midplane, with $|\alpha|$ increasing with $|z|$ from 0 at $z = 0$ to a maximum at $|z| = h/2$, and then decreasing to zero as $|z| \rightarrow \infty$ (remembering that we only explicitly model the region $z \geq 0$). Because of the symmetry of Eqs. (1) and (2), if \mathbf{B} is a solution, then $-\mathbf{B}$ is also a solution.

We take $\xi = O(1)$, assuming that there is no catastrophic α -quenching (e.g. Brandenburg & Subramanian 2005). The models were computed with $\xi = 1$, and the field strength then scales as $\xi^{-1/2}$. The turbulent speed that enters B_{eq} is taken to be equal to the speed of sound as adopted in the gas dynamical model. The gas density $\rho(x, y, 0)$ is taken from the gas dynamical model described in Sect. 3.1. We extend this away from $z = 0$ by writing

$$\rho(x, y, z) = \frac{\rho(x, y, 0)}{\cosh(|z|/h)}. \quad (4)$$

The magnitude of the gas density is relatively unimportant in our model (where the Lorentz force is not included into the

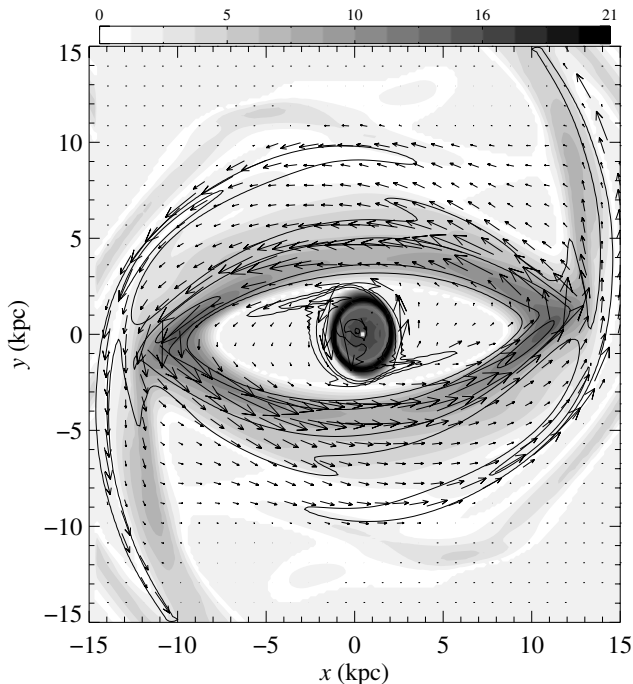


Fig. 4. Energy density contours and vectors of the regular magnetic field \mathbf{B} from Model 2 (see Table 1), both at $z = 0$, are shown together with gas number density represented with shades of grey. The contours shown correspond to approximately 0.1, 0.6 and 3.0 times the rms value; the length of the vectors is proportional to B^2 . The scale bar at the top of the frame refers to the gas number density in the units of hydrogen atoms per cm^3 .

Navier-Stokes equation) as it affects only the magnitude of the magnetic field in the steady state, via Eq. (2), but not its spatial distribution. The only aspect where the magnitude of gas density plays a role is the Faraday depolarization and, hence, the modelled distribution of polarized intensity. This effect is, however, relatively weak at $\lambda = 3\text{--}6$ cm and it is plausible that other depolarization effects (e.g., Faraday dispersion) are more important in the real galaxy. The gas density in our model is shown in Fig. 4.

The gas velocity in the plane $z = 0$, $\mathbf{u}(x, y, 0)$, is also taken from the gas dynamical model. For convenience, we split this into rotational and non-circular parts,

$$\mathbf{u}(x, y, 0) = \Omega(r)r\hat{\phi} + \mathbf{v}(x, y, 0), \quad (5)$$

respectively, where $r = (x^2 + y^2)^{1/2}$ is axial distance.

We then introduced two significant modifications. We found that, in the gas dynamical model, $\Omega(r)$ increases very rapidly towards the rotation axis (very approximately, as $1/r$). The gas dynamical model appears to handle this feature satisfactorily, but it causes significant numerical problems for the dynamo code at attainable numerical resolution. Thus Ω was softened by introducing an explicit parabolic profile within a radius of 2.1 kpc, with the maximum of Ω truncated to $110 \text{ km s}^{-1} \text{ kpc}^{-1}$ (as compared to $1730 \text{ km s}^{-1} \text{ kpc}^{-1}$ at $r = 0.013$ kpc, the smallest distance from the axis in the gas dynamical model used). This modification can be expected to reduce the magnetic field strength in regions close to the galactic centre, but as this region is not well resolved by the radio observations, we cannot in any case make a comparison between these and the computed magnetic field.

Table 1. Parameters of models discussed in the text, as defined in Sect. 3.2. In all the models, the angular speed of the bar is $\Omega_p = 16.16 \text{ km s}^{-1} \text{ kpc}^{-1}$ with the corotation radius at 15.5 kpc.

Model	R_α	η_0 [$10^{26} \text{ cm}^2 \text{ s}^{-1}$]	q_η	r_η [kpc]	f_η	c_s [km s^{-1}]
1	3.0	1.0	3	3.0	0	10
2	3.0	1.0	3	1.5	2	10
3	0.0	1.0	3	1.5	2	10
4	2.7	2.5	3	1.5	2	10
5	3.0	2.0	3	1.5	2	10
6	3.0	1.0	3	1.5	2	30

Further, we continued the velocity field above the disc by introducing z -dependence into the horizontal velocity components via

$$\mathbf{u}(x, y, z) = \frac{\mathbf{u}(x, y, 0)}{\cosh(|z|/1.2 \text{ kpc})}, \quad (6)$$

and $u_z = 0$ everywhere.

In order to model a galaxy surrounded by near-vacuum, we allow the magnetic diffusivity to become large high in the halo (Sokoloff & Shukurov 1990),

$$\eta = \eta_0 \begin{cases} 1, & |z| \leq h, \\ 1 + (\eta_1 - 1) \left[1 - \exp\left(-\frac{|z| - h}{1.5 \text{ kpc}}\right) \right]^2, & |z| > h, \end{cases}$$

where η_0 and η_1 are constants; thus $\eta = \eta_0$ near the disc midplane and $\eta \rightarrow \eta_0\eta_1$ in the halo region ($|z| > h$). We adopted a nominal $\eta_1 = 2$ – larger values led to numerical difficulties. A conventional value of η_0 is $10^{26} \text{ cm}^2 \text{ s}^{-1}$; however, we also considered models with values larger than that – see Table 1. In order to reproduce polarized radio maps of NGC 1365 in sufficient detail, we had to introduce further spatial variation in η . Following Moss et al. (2001), we have assumed that the turbulent diffusivity is enhanced by the shear of the nonaxisymmetric velocity according to

$$\eta_0 \propto \left(1 + f_\eta \frac{S}{S_{\max}} \right), \quad S = \left| \frac{\partial u_x}{\partial y} \right| + \left| \frac{\partial u_y}{\partial x} \right|,$$

where S_{\max} is the maximum value of S . The effect of $f_\eta \neq 0$ is, firstly, to broaden magnetic structures near the spiral arms, and, secondly, to reduce the central peak of magnetic field. The values of f_η adopted are shown in Table 1. We did not consider a similar enhancement in α as Moss et al. (2001) found it to be unimportant. The values of f_η that were sufficient to produce realistic magnetic fields in spiral arm were still too small to reduce the central maximum of magnetic field to an acceptable level. Therefore, we introduced an additional enhancement of η in the central part of the galaxy, multiplying η_0 by $q_\eta \exp(-r^2/2r_\eta^2)$; the values of q_η and r_η are given in Table 1 for each model studied.

Clearly, we have made a number of rather arbitrary choices, in particular when extending the two dimensional gas dynamical model into three dimensions. Our overall impression from a substantial number of numerical experiments is that the overall nature of our results does not depend very strongly on these choices.

At $z = z_{\max}$, and on $x, y = \pm L$, the boundary conditions are $B_x = B_y = 0$. On $z = 0$, $\partial B_x/\partial z = \partial B_y/\partial z = 0$, $B_z = 0$, and so the integration of $\nabla \cdot \mathbf{B} = 0$ gives the values of B_z on the other boundaries. These are conservative boundary conditions on B_x

and B_y , in that they will increase the field gradients and thus raise the threshold for dynamo action to occur.

We nondimensionalize the problem in terms of the length $L = 15$ kpc, time h^2/η_0 and magnetic field B_{eq} . Given that the velocity field, including the angular velocity, is given by the dynamical model, the only free dynamo parameter is α_* ; the corresponding dimensionless parameter is

$$R_\alpha = \frac{\alpha_* h}{\eta_0}, \quad (7)$$

where α_* is defined in Eq. (3). The dynamo action prevents magnetic field from decay for values of R_α exceeding about 1 for $\eta_0 = 10^{26} \text{ cm}^2 \text{ s}^{-1}$; the critical value of R_α increases roughly proportionally to η_0 .

Henceforth, we will use dimensionless variables, unless explicitly otherwise stated; the units of gas number density and magnetic field strength are 44 cm^{-3} and $30 \mu\text{G}$, respectively.

4. Results

The gas dynamical and dynamo models described above together yield the gas density and the distribution of the large-scale magnetic field in the galaxy. The distribution of magnetic field in the galaxy plane resulting from Model 2 (introduced in Table 1), which we argue below to be our best model, is shown in Fig. 4. Given the distribution of the cosmic rays, we can now construct synthetic radio observables in order to assess the quality of the model. We have computed synthetic radio polarization maps at wavelengths of 3.5 cm and 6.2 cm using the dynamo generated magnetic field and the gas density, and compared them with the observed radio maps. Details of this procedure are given in Appendix A. Since we do not model turbulent magnetic fields, we are unable to calculate the total radio intensity and to estimate the degree of polarization from the model.

We considered several models for the number density of cosmic rays, n_{cr} , which we discuss in Sect. 5.1. For all but one of the dynamo models listed in Table 1 we find that the simplest possible choice, $n_{\text{cr}} = \text{const}$, provides the best fit to the observed data, regardless of the other quantities adopted. The larger value of r_η in Model 1 produces a relatively weak magnetic field throughout a large central region compared with that at the ends of the bar. In order to fit the observed central peaks of polarized intensity, P , an implausible non-uniform distribution of n_{cr} would be required in this model. Specifically, the cosmic ray distribution required to reconcile this model with observations would have a high peak within 3 kpc of the centre where magnetic field strength is minimum. For the other dynamo models, any plausible non-uniform distribution of n_{cr} produces too strong a central maximum of P relative to all other structures. In particular, the polarized intensity in the spiral arms is almost lost in models with non-uniform n_{cr} , being far weaker than that within 1–2 kpc of the centre. Since we have truncated the angular velocity at $r < 2.1$ kpc, the untruncated differential rotation would lead to an even stronger discrepancy.

Our synthetic maps do not include any depolarization effects due to random magnetic fields (see Burn 1966; Sokoloff et al. 1998), although they allow fully for depolarization by the regular magnetic fields (differential Faraday rotation and beam depolarization). In order to include Faraday depolarization effects due to the large-scale magnetic field, we assumed a nominal constant ionization fraction of $X = n_e/n = 0.1$, corresponding to a thermal electron density of 0.1 of the total gas density obtained from the gas dynamical simulations as described in Sect. 3.2. Guided

by analogy with the Milky Way, where the average total gas density is 1 cm^{-3} whereas the thermal electron density is 0.03 cm^{-3} , a smaller value of X might be appropriate. We show results for X close to this value in Sect. 4.1. In Sect. 5.5, we discuss the effect of variations in X and argue that $0.01 \lesssim X \lesssim 0.2$.

We used two main techniques to compare the synthetic maps with observations and therefore to select the optimal magnetic field model. We chose to use the $\lambda 6.2$ cm map of polarized intensity in the analysis since it has the best signal-to-noise ratio. All model data, including synthetic radio maps, have been smoothed (in terms of the Stokes parameters Q and U) to match the resolution of the observations. In Sect. 4.2 we compare the distributions of polarized intensity on cuts along various paths in the plane of the sky. In Sect. 4.3 we analyse the difference between the computed and observed polarized intensities in two dimensions. In addition, we compare the orientations of the magnetic B -vectors obtained from the observed and synthetic Stokes parameters (Sect. 4.5).

To rotate the model galaxy to the position of NGC 1365 in the sky, we took the inclination angle $i = 46^\circ$ and the position angle of the galaxy’s major axis (i.e. the intersection of the sky plane and the galaxy plane) $\text{PA} = 222^\circ$, which are those assumed in obtaining the rotation curve for our (favoured) gas dynamical model. Results are quite sensitive to these values, and it is possible that a reappraisal could result in noticeable changes.

4.1. Synthetic polarization maps

Overall, Model 2 (specified in Table 1) appears to provide the best fit to the observed polarization map; Model 4 is only slightly worse – see Sect. 4.2. Contours of B^2 shown in Fig. 4 indicate that the regular magnetic field is stronger in the bar region where gas density is large, and outside the regions of high density in the spiral arms. There are magnetic features apparently unrelated to the density distribution [e.g., those passing through the positions $(x, y) \approx (-5, 8), (5, -8)$]; they are presumably formed by a locally enhanced velocity shear. The magnetic field has a deep minimum within the bar, mainly produced by the density deficiency in that region. Other important features clearly visible in Fig. 4 are the magnetic field enhancements in the dust lane region, where magnetic field is amplified by both compression and shear, and the prominent central peak.

The synthetic polarization map for this model is shown in Fig. 5. This can be compared directly with the observed map in the right-hand-panel of Fig. 1; the maps (and all other maps we show) are at a similar scale to facilitate the comparison; we make this comparison more quantitatively in Sect. 4.3. Our models have a high degree of symmetry, whereas the “real” NGC 1365 is only approximately symmetric; since the observed map looks more regular on the eastern side, we shall mostly refer to that part of the galaxy unless stated otherwise. Despite the difference in symmetry, there is broad agreement between these two maps; for example, both have a deep minimum of P near the bar’s major axis where gas density is low, and both have the magnetic spiral arms displaced from the gaseous ones (although both magnetic arms are displaced to larger radii in the synthetic map, only one arm is so displaced in the observed map). The minimum of the synthetic P in the bar (corresponding also to a minimum of magnetic field within the bar, as seen in Fig. 4), is broader than of the observations (see Sect. 4.2). The reason for this is the very low gas density in this region, leading to weaker magnetic fields via Eq. (2). This feature is further discussed in Sect. 6 where we argue that the gas dynamical model underestimates significantly the amount of molecular gas in the bar region. Synthetic P is large both to the north and south of the bar

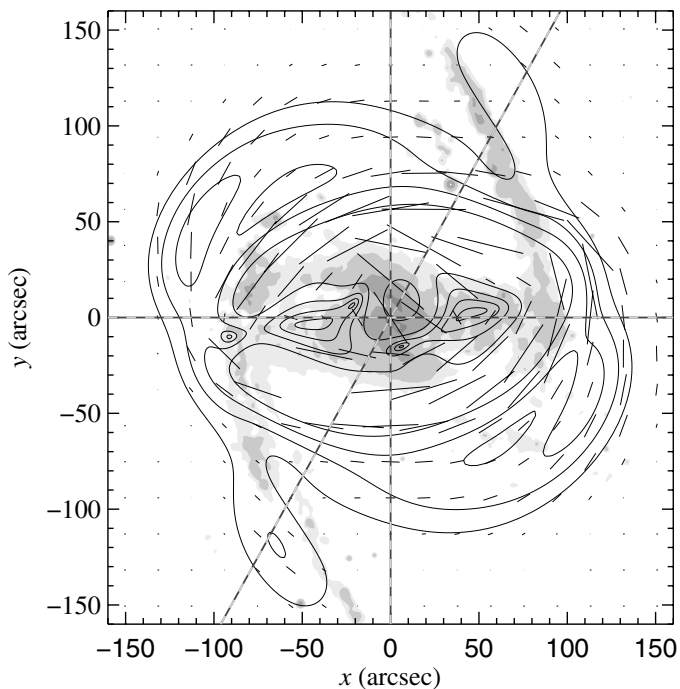


Fig. 5. A synthetic map of polarized synchrotron intensity (contours) and polarization planes at $\lambda 6.2$ cm, resulting from Model 2 (see Table 1) assuming that $n_{\text{cr}} = \text{const}$, are shown superimposed on the optical image of the galaxy NGC 1365 (shown in only a few shades of grey for clarity). The synthetic map has been smoothed to the resolution of $25''$ to match that of the observed map shown in Fig. 1. The contour levels shown are approximately $(1, 3, 6, 12, 32) \times P_{\text{max}}/45$, where P_{max} is the maximum of P in the synthetic map. Dashed lines show the position of cuts discussed in Sect. 4.2.

major axis. In particular, the model reproduces a maximum of P upstream of the bar major axis, centred in the $\lambda 6.2$ cm map of Fig. 1 at (RA = $03^{\text{h}} 33^{\text{m}} 40^{\text{s}}$, Dec = $-36^{\circ} 09' 00''$). These maxima apparently arise from slightly enhanced velocity shear (that locally amplifies magnetic field) rather than from local density maxima. We also note maxima of P near the ends of the bar and the beginning of the spiral arms, at (RA = $03^{\text{h}} 33^{\text{m}} 45^{\text{s}}$, Dec = $-36^{\circ} 08' 15''$) and (RA = $03^{\text{h}} 33^{\text{m}} 28^{\text{s}}$, Dec = $-36^{\circ} 08' 30''$). We note that the observed total emission (not shown here; see Beck et al. 2005) is related to gas density in a rather straightforward manner being correlated with the gas density. The fact that this is not the case with the polarized intensity (as seen in both observed and synthetic maps) confirms that the observed regular magnetic field is not frozen into the gas, apparently being affected by the dynamo action.

4.2. Cuts through polarization maps

We found that comparisons can be usefully quantified and detailed using the cuts in the sky plane mentioned above. We show cuts only through the map at $\lambda 6.2$ cm because this map has higher signal-to-noise ratio and includes the large-scale emission fully. However, depolarization is significant at this wavelength (see Sect. 2) and has to be taken into account when comparing the model and observations. We use cuts through the centre of the galaxy at position angles PA = 0° , -90° and -31° , where PA is measured counterclockwise from the north as shown in Fig. 5. (The angle -31° is chosen so that the cut goes through the spiral arms; this corresponds roughly to a diagonal in the computational frame of Fig. 4.) The positions

of these cuts are shown in Fig. 5. The synthetic P has been normalized to make the mean difference between that and the observed P approximately zero. We have superimposed another profile from cuts through synthetic maps which represents both P at $\lambda 3.5$ cm with our favoured value of $X = 0.1$, and also at $\lambda 6.2$ cm with $X = 0.032$ (incidentally, this is close to the mean ionization degree of the warm diffuse gas in the Milky Way). The coincidence of these two cuts is due to equivalent Faraday depolarization, which depends directly on the quantity $\psi(z) \propto \lambda^2 X \int_{-\infty}^{\infty} n B_{\parallel} dz$ along the line of sight towards an observer (see Appendix A). Here B_{\parallel} is the line of sight field component and $n_e = Xn$, therefore $\lambda^2 X = \text{const}$ identifies equivalence in depolarization. We see that this value is about the same in both cases (i.e. $6.2^2 \times 0.032 \approx 3.5^2 \times 0.1$). The difference between the polarization for these two possibilities is then just a λ -dependent scale factor.

The cuts are presented in Figs. 6–8 for the best-fit Model 2 and also for Model 4. The latter model has the background turbulent magnetic diffusivity η_0 enhanced by a factor of 2. This leads to a significantly smoother, less structured distribution of P . Thus, comparison of Models 2 and 4 allows us to suggest that the effective turbulent magnetic diffusivity in the interstellar gas of barred galaxies is, on average, close to $\eta_0 = 10^{26} \text{ cm}^2 \text{ s}^{-1}$. This value is typical of spiral galaxies in general and is that obtained if the turbulent speed v_t is close to 10 km s^{-1} and the turbulent scale is about $l = 0.1 \text{ kpc}$; $\eta_0 \approx \frac{1}{3} l v_t$.

Our model neglects depolarization due to random magnetic fields which can reduce the value of P in the central parts more strongly than in the outer galaxy and therefore affect the relative height of the central peaks in Figs. 6–8. Depolarization due to internal Faraday dispersion reduces the degree of polarization to

$$p = p_0 \frac{1 - e^{-S}}{S}, \quad (8)$$

where $S = 2\sigma_{\text{RM}}^2 \lambda^4$ with $\sigma_{\text{RM}}^2 = 2C_1^2 \langle b^2 \rangle \langle n_e^2 \rangle dL$ the variance of the Faraday rotation measure. Here C_1 is the dimensional constant appearing in the definition of the Faraday rotation measure (see Appendix A), b is the turbulent magnetic field, angular brackets denote averaging (the fluctuations in magnetic field and thermal electron density are assumed to be uncorrelated), d is the turbulent scale and L is the path length (Sokoloff et al. 1998). The best available estimate of the random magnetic field in the central region of NGC 1365, $b \approx 40 \mu\text{G}$, follows from the total synchrotron intensity assuming equipartition between cosmic rays and magnetic fields (see however Sect. 5.1 for a discussion of the validity of this assumption). For $n_e = 0.03 \text{ cm}^{-3}$, $d = 0.1 \text{ kpc}$, $L = 1 \text{ kpc}$ and $\lambda = 6.2 \text{ cm}$, we then obtain $S \approx 6$, implying that this mechanism can depolarize the central peak significantly, giving $p/p_0 \approx 0.2$. Since the height of the secondary peak should also be affected by depolarization, albeit to a lesser extent, we expect that the ratio of the two peaks will be reduced by a factor smaller than five. We note, however, that this estimate is uncertain since the number density of thermal electrons, their filling factor, turbulent scale and other parameters are not known well enough. An alternative is to assess the importance of this depolarization effect by comparing polarized intensities at $\lambda 6.2$ cm and $\lambda 3.5$ cm. The ratio of the central peak to the secondary ones at $\lambda 3.5$ cm is about 6–8, as opposed to 2–3 at $\lambda 6.2$ cm. The difference can be attributed to Faraday depolarization (by both regular and random magnetic fields). Assuming that Faraday depolarization at $\lambda 3.5$ cm is negligible, we conclude that it can reduce the degree of polarization at $\lambda 6.2$ cm by a factor as large as 4, which is consistent with the analytical estimate.

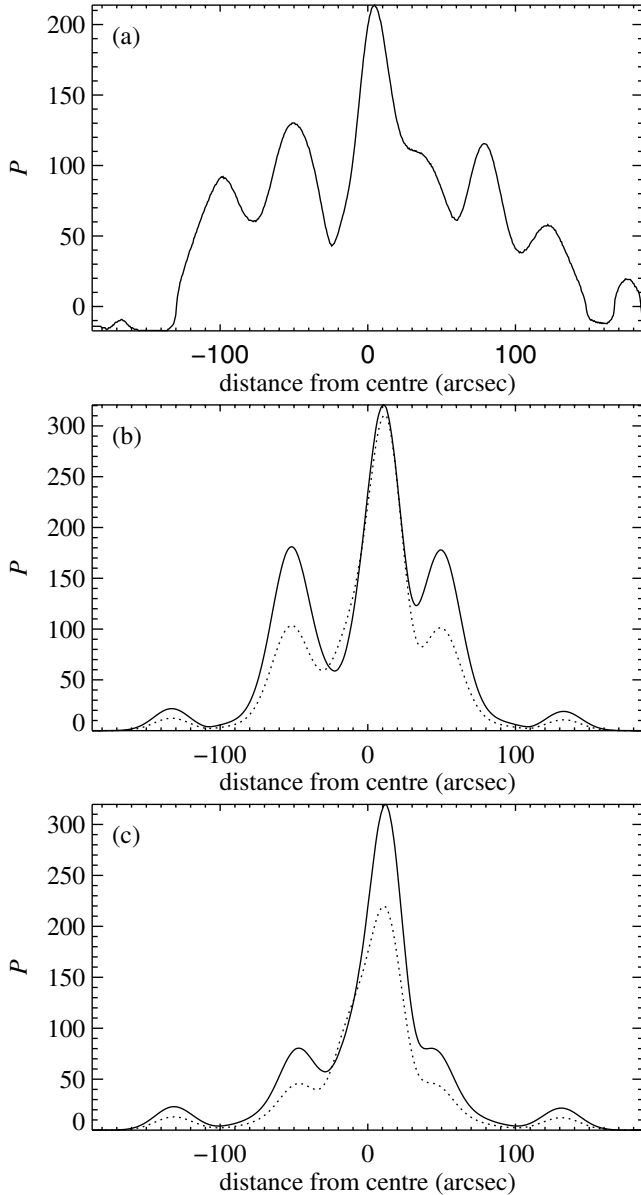


Fig. 6. Cuts, at position angle -31° passing through the galactic centre (left to right in the plots corresponds moving from south-east to north-west in the sky), through polarized intensity maps at $\lambda 6.2$ cm smoothed to $\text{HPBW} = 25''$, for **a)** the observed map, and synthetic maps from **b)** Model 2 and **c)** Model 4, both for $n_{\text{cr}} = \text{const}$. In panels **b)** and **c)**, the synthetic profiles for $\lambda 6.2$ cm and $\lambda 3.5$ cm are shown solid and dotted, respectively; the difference is due to Faraday and beam depolarization for the assumed ionization degree $X = 0.1$. The units of P are as in Fig. 1 for **a)** and arbitrary in **b)** and **c)**, but adjusted to fit a similar range. The dotted profiles for $\lambda 3.5$ cm with $X = 0.1$ also correspond to P at $\lambda 6.2$ cm with $X = 0.032$.

We conclude that the relative height of the central peak in the synthetic cuts of Figs. 6–8 would be reduced by Faraday dispersion, although this is difficult to estimate accurately.

Given the above uncertainties in the amount of depolarization, all three cuts for Model 2 are similar to those observed. In particular, the relative heights of the peaks in P and, more importantly, the positions of both maxima and minima are remarkably realistic. The characteristic feature of this model is that η is further enhanced by a factor of $q_\eta \approx 3$ in the inner region of NGC 1365, $r \lesssim 3$ kpc. This enhancement can be due to a higher rate of star formation, and hence more hot gas, with a

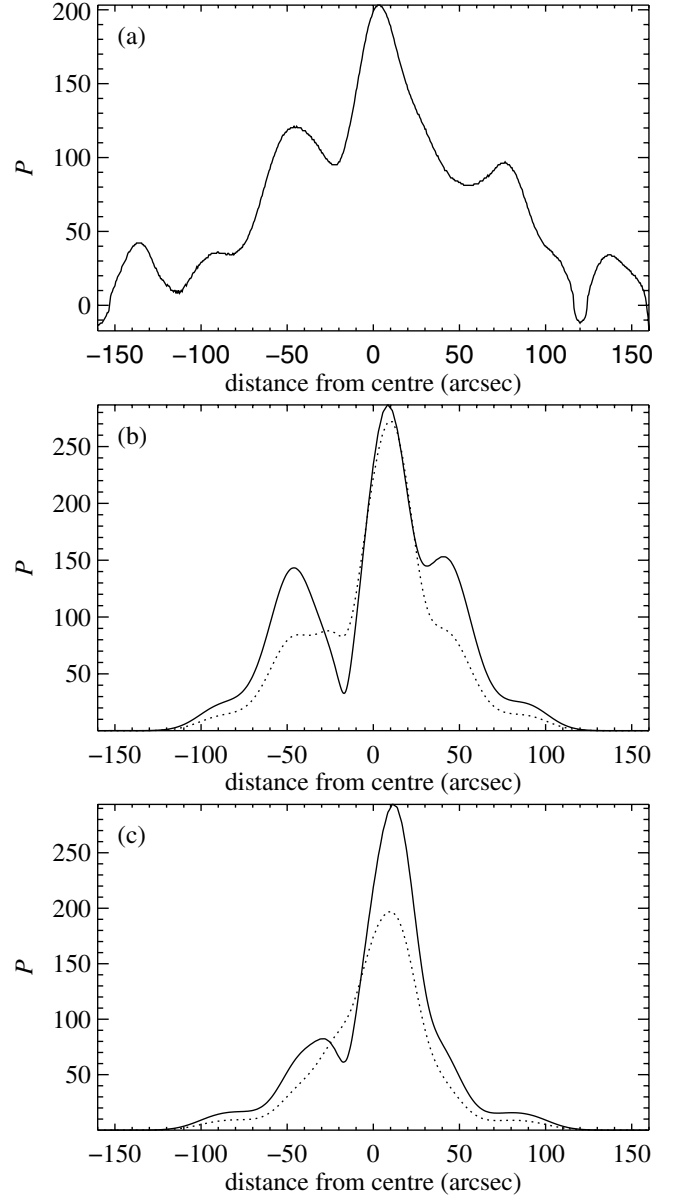


Fig. 7. As in Fig. 6, but at position angle 0° (left to right is south to north in the sky).

correspondingly higher speed of sound, which would allow the turbulent speed to be larger than elsewhere.

The Model 2 cut at $\text{PA} = -31^\circ$ (Fig. 6), which passes through the spiral arms, shows an encouraging agreement with observations. For example, B has a maximum slightly outside the northern arm in both this model and the real galaxy. However, the outermost maxima produced by the spiral arms are slightly too far away from the centre in the model. As illustrated in Fig. 6b, the relative heights of the peaks at $\lambda 6.2$ cm are significantly affected by Faraday rotation even for $X = 0.1$, where they clearly differ by more than just a scale factor between $\lambda 6.2$ cm and $\lambda 3.5$ cm.

The cut at $\text{PA} = 0$ (Fig. 7) exhibits similar degree of agreement with the observations. The main deficiency of the model here is the too narrow distribution of P (the magnetic structure of the model is too poor outside the bar) and the minimum is too deep near the centre of the cut.

The cut at $\text{PA} = -90^\circ$ in the synthetic map, shown in Fig. 8, has a central maximum that is too narrow (or off-centre minima that are too broad). This difference results in the deep minima

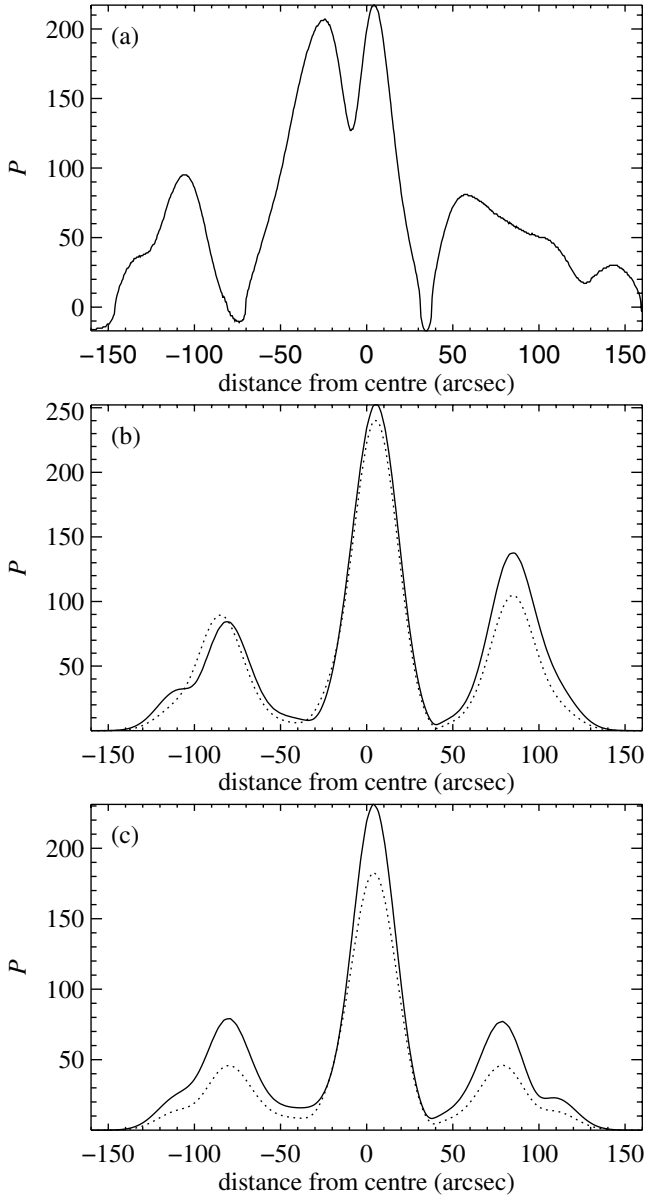


Fig. 8. As in Fig. 6, but at position angle -90° (left to right is east to west in the sky).

in the difference parameter δ discussed in Sect. 4.3. The sharp minimum in the observed cut near the centre is a result of beam depolarization; it occurs in the synthetic cuts as well, but is removed by smoothing.

Model 2 seems to be almost optimal. The model could be fine tuned by changing η_0 and r_η within the ranges $(1-2) \times 10^{26} \text{ cm}^2 \text{ s}^{-1}$ and 1.5–3, respectively. For example, the secondary peaks in the PA = 0 cut decrease in strength in Model 4. Further, increasing n_{cr} by a factor of 2 within the central 1.5 kpc would make the central peak higher. However, we have not made such *post hoc* adjustments.

4.3. The difference maps

To obtain a global comparison of the models and observations, we produced maps of the difference between the observed and synthetic polarization at $\lambda 6.2 \text{ cm}$, with the synthetic polarization scaled to make the mean difference approximately zero; this

measure was further normalized by dividing the difference by the appropriately normalized noise level of the observed map giving

$$\delta = \frac{(1.4P/P_{\text{max}})_{\text{model}} - (P/P_{\text{max}})_{\text{obs}}}{(\sigma_P/P_{\text{max}})_{\text{obs}}} \quad (9)$$

Thus, all comparisons were performed pointwise after their reduction to the common resolution $25''$ – this is quite a stringent test of the model. The result is shown in Fig. 9 for Model 2.

Since the models – unlike the real galaxy – possess perfect symmetry, the difference can hardly be uniformly small: a perfect fit in one half of the galaxy would produce significant systematic discrepancy in the other half. With this caveat, the difference map shows an acceptable global agreement of the model with observations, in that it does not show much of the basic morphological elements of the galaxy. The normalized relative difference is about 6–14 in four spots observed to the east, south and north-west of the galactic centre, indicating that synthetic polarized intensity is too small upstream of the dust lanes and at two positions at the inner edge of the western spiral arm. Otherwise, $|\delta| \lesssim 4$ across the whole field of view. Given the limited scope of our model (e.g., it does not include any turbulent magnetic fields which can produce polarized radio emission where they are anisotropic), we consider this degree of agreement to be acceptable. We discuss in Sect. 5.1 a cosmic ray distribution that would provide an almost perfect fit of Model 2 to observations.

4.4. Faraday rotation

We can use polarized intensity (as in the comparisons above) to probe the distribution of the large-scale magnetic field strength, and also to deduce the orientation of the magnetic field in the plane of the sky (via polarization vectors). However, knowledge of this quantity does not determine the field direction. The Faraday rotation measure RM is sensitive to the direction of the magnetic field, but the observed RM map is very patchy because of the lower signal-to-noise ratio at $\lambda 3.5 \text{ cm}$. Therefore, we used RM data only to establish a minimum acceptable degree of gas ionization.

4.5. Magnetic field structure

An analysis of the observed global magnetic structure in NGC 1365 that is sensitive to the direction of magnetic field was performed by Beck et al. (2005) by fitting the polarization angles obtained from multi-frequency observations. This analysis provides the large-scale magnetic field expanded into Fourier series in the azimuthal angle. Their results indicate the presence of a significant component with the azimuthal wave number $m = 1$ at almost all distances from the galactic centre. However, our underlying gas dynamical model has even symmetry in azimuth, so that modes with odd values of m do not occur in the modelled magnetic field. The contribution of the $m = 1$ mode to those Fourier expansions is more important than just producing the overall asymmetry. In particular, superposition of various azimuthal modes produces local magnetic features at kiloparsec scale which are lost if only even modes are retained in the observed structure to facilitate comparison with the model. Therefore, we did not find it useful to compare the modelled and observed magnetic structures in this manner. (The presence of unmodelled odd- m structure was also a feature of our study of NGC 1097 in Moss et al. 2001.)

We instead compare directly the orientation of the magnetic field vectors in the observed and synthetic polarization maps.

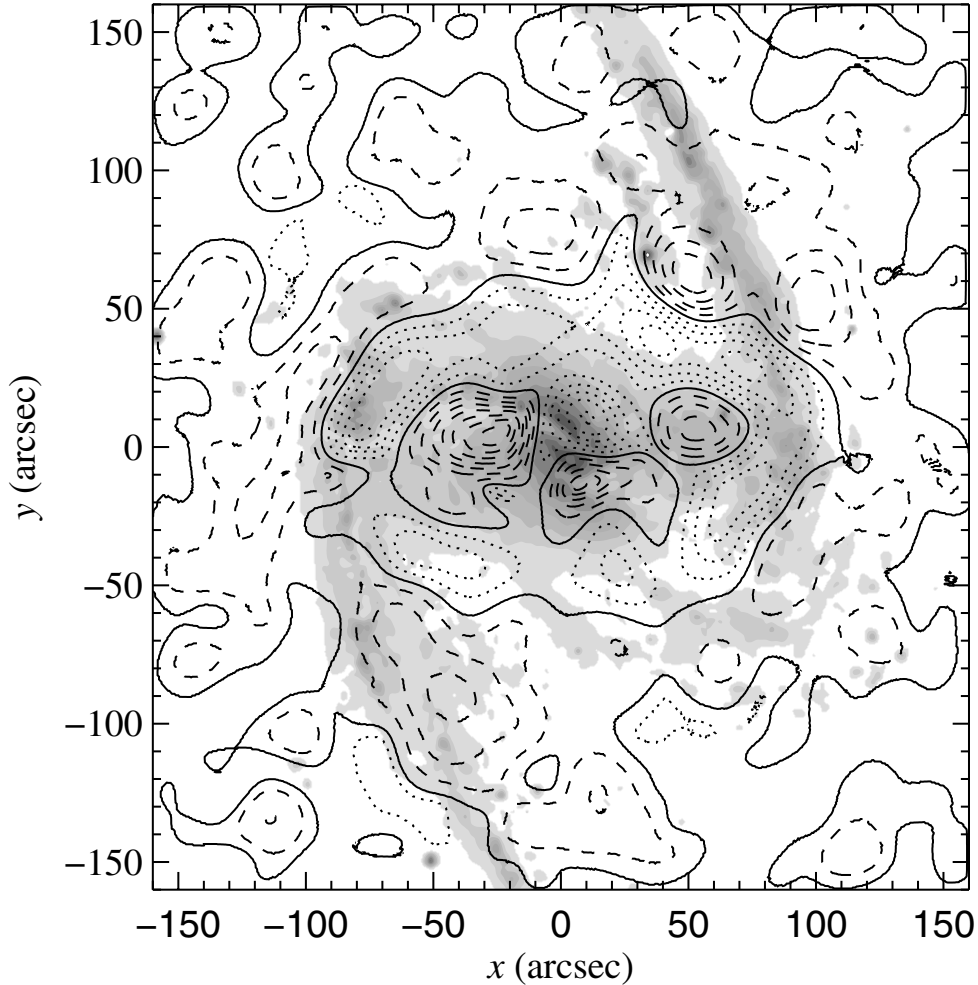


Fig. 9. The difference δ between normalized synthetic and observed polarization maps at $\lambda 6.2$ cm, as defined in Eq. (9), superimposed on the optical image of NGC 1365. The contour spacing is 2, with the zero contour shown solid, negative values of δ dashed, and positive, dotted.

Comparison of two-dimensional vector fields is difficult. We could approach this by taking cuts through maps of the magnetic field orientation angles, as was done with the polarized intensity. However, a small shift in a feature such as a shock front can result in drastic differences between any such cuts made parallel to the front.

In Fig. 10 we show the orientation of both the synthetic and observed magnetic field vectors obtained directly from the corresponding Stokes parameters; points below 3 times the rms noise level are neglected in the observed maps. Agreement between model and observations is reasonable in the top left and bottom right quadrants near the bar (and partly further out), whereas the differences are quite large in the other regions. The difference is especially large near beginning of the spiral arms. The mean value of the difference between the observed and modelled polarization angles is 33° , and its standard deviation is 25° . For comparison, the errors in the observed polarization angle range from 2 to 10 degrees.

The overall difference is that the model polarization vectors are arranged into a more elliptical pattern around the bar than the observed ones, which exhibit a more circular configuration (and have almost constant pitch angles). It seems that the non-axisymmetric distortion due to the bar is weaker in the observed magnetic field than in the model. This could be because the magnetic field is coupled to a warm gas component which has less

response to the bar's potential than cold gas and stars. We made a comparison similar to that in Fig. 10 but for Model 6, where the speed of sound is 30 km s^{-1} (see Table 1). The resulting gas dynamical model illustrated in Fig. 2 (right hand panel) has a more uniform density distribution and weaker deviations from axial symmetry. The improvement in the magnetic pattern was only marginal, and so the reason for this discrepancy remains unclear.

5. Sensitivity to parameters, and implications of the dynamo models

In this section, we discuss how synthetic radio maps are affected by various changes in our model. This allows us to infer useful information about the interstellar medium in the galaxy.

5.1. Distribution of cosmic rays

In order to calculate the synchrotron intensity, we need to specify the number density of cosmic ray electrons. There are no direct measurements of this quantity in external galaxies, and there are no sufficiently detailed theories that might supply it. Therefore,

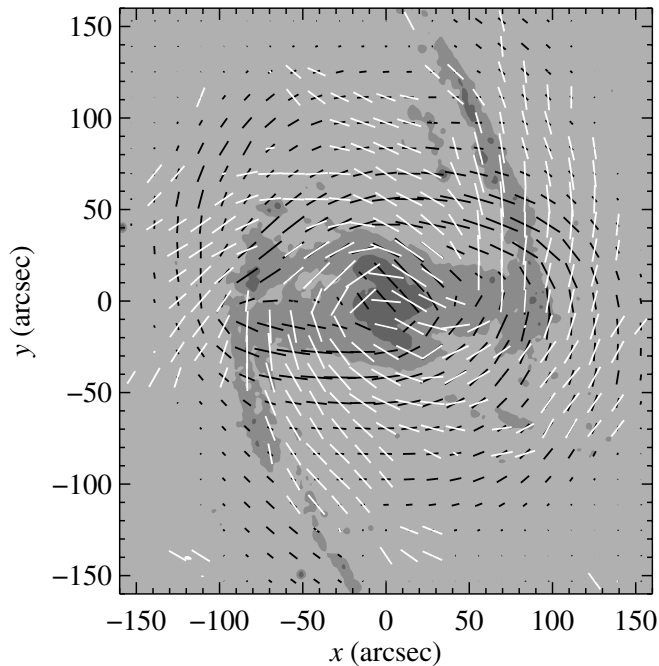


Fig. 10. Orientations of the B -vectors of polarized emission obtained from the observed (white) and synthetic (black, Model 2) Stokes parameters at 26.2 cm. The vector lengths are proportional to \sqrt{P} . For the observed B -vectors, positions where polarized intensity is weaker than three times the noise level, $P < 3\sigma_P$, are neglected.

empirical models for the cosmic ray number density n_{cr} were studied with

- (i) $n_{\text{cr}} = \text{const}$,
 - (ii) $n_{\text{cr}} \propto \sqrt{I}$,
 - (iii) $n_{\text{cr}} \propto p^{-1}$,
- (10)

where I is the observed total radio intensity and p is the percentage polarization of synchrotron emission at short wavelengths; models (ii) and (iii) are motivated below. Thus, we make an attempt to relate n_{cr} to various observable quantities. The first model is the simplest possible, and it attributes all the variation in synchrotron intensity to that of the magnetic field. The motivation for model (ii) is that, if cosmic rays are in equipartition with the total magnetic field, $n_{\text{cr}} \propto B_{\text{tot}}^2$, then the total intensity of synchrotron emission is roughly proportional to n_{cr}^2 . Model (iii) relies again on the idea of equipartition between cosmic rays and magnetic fields, but now we use expression $p \approx p_0 B^2 / B_{\text{tot}}^2$ (Burn 1966; Sokoloff et al. 1998) to estimate n_{cr} as $n_{\text{cr}} \propto B_{\text{tot}}^2 \approx B^2 p_0 / p$, where $p_0 \approx 0.75$ and B can be taken from our dynamo model. This rough estimate neglects any depolarization effects and any contribution of anisotropic random magnetic fields to polarized intensity (Sokoloff et al. 1998).

As illustrated in Fig. 11, the major and universal effect of any plausible non-uniform distribution of n_{cr} is to enhance the central maximum in P , so that the peaks in the outer parts become relatively insignificant. Most importantly, any signature of the spiral arms almost disappears. If the synthetic polarized intensity is rescaled to fit that observed in the spiral arms, the central peak becomes unacceptably broad and high. Using $n_{\text{cr}} \propto B^2 / p$ instead of p^{-1} as in model (iii) does not improve the situation. Similarly, it does not help if we use $n_{\text{cr}} \propto B_{\text{tot}}^2 = B^2 + 4\pi\rho v^2$, assuming that the random magnetic field is in equipartition with turbulent energy. Since models (ii) and (iii) involve the assumption of energy equipartition (or pressure balance) between

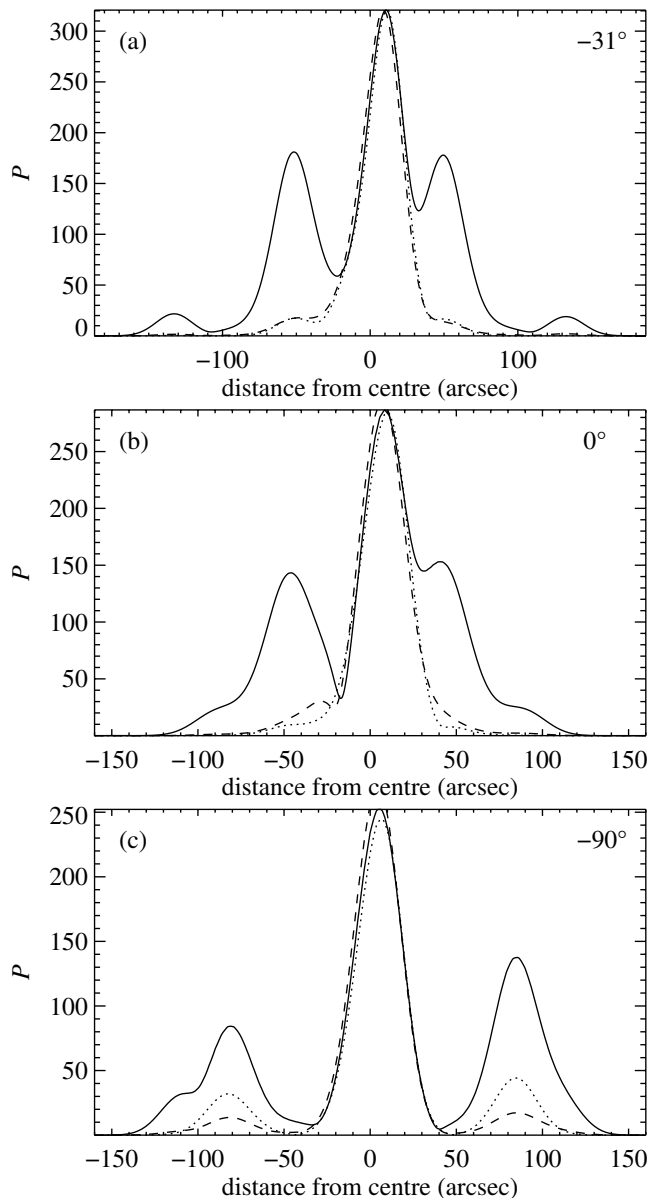


Fig. 11. Cuts through radio maps for various models of cosmic ray distribution as defined in Eq. (10); the position angle of the cut is indicated in the upper right corner of each panel: **a)** -31° , **b)** 0° , and **c)** -90° . The solid lines are for Model 2, i.e., with $n_{\text{cr}} = \text{const}$, and are identical to those in Figs. 6b–8b; the other two cuts in each panel are for model (ii) $n_{\text{cr}} \propto \sqrt{I}$, dashed; and model (iii) $n_{\text{cr}} = p^{-1}$, dotted.

cosmic rays and magnetic fields, we conclude that our results do not suggest this type of relation between cosmic rays and magnetic fields at large scales.

We can think of several plausible explanations for this perhaps surprising result. It may be that some fraction of the polarized emission in the outer galaxy is produced by anisotropic magnetic fields which are not modelled. We do not consider this to be a very plausible option as this would require the anisotropy to be larger in the outer galaxy and in the spiral arms, rather than in the region of the central peak. Meanwhile, velocity shear, which might produce the anisotropy, is stronger in the inner bar region. More plausibly, cosmic ray diffusion makes their distribution smoother than that of the magnetic field. With the cosmic ray diffusivity of $K \approx 10^{29} \text{ cm}^2 \text{ s}^{-1}$ and the confinement time

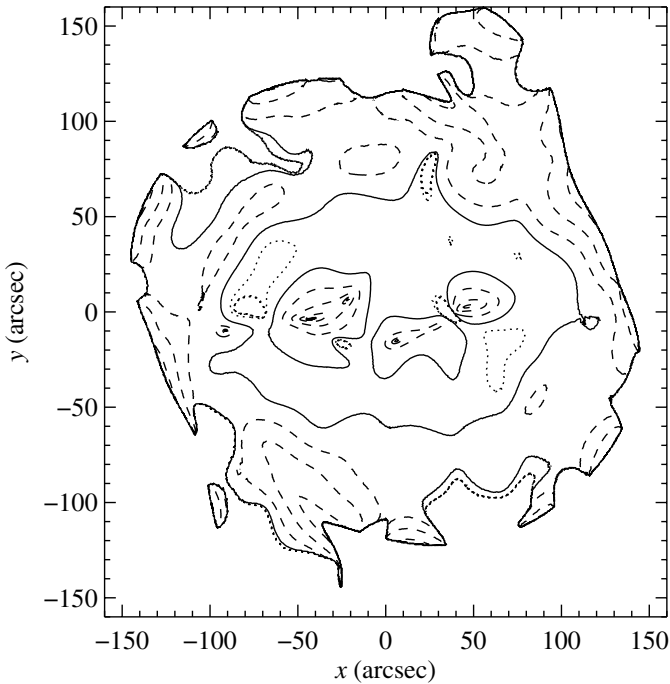


Fig. 12. A map of the ratio of polarized intensity observed at $\lambda 6.2$ cm to the synthetic P obtained from Model 2 with $n_{\text{cr}} = \text{const}$. This ratio can be used to assess the variation of n_{cr} required to achieve a perfect fit to observations (neglecting any anisotropy of the turbulent magnetic fields and any contribution of a hypothetical galactic halo to the polarized emission). The contour at level unity is shown solid, the other contours are at levels 3^n , with negative and positive integer values of n ; contours above (below) unity are shown dashed (dotted).

$\tau \approx 10^6$ yr, their distribution would be rather homogeneous at scales $(K\tau)^{1/2} \approx 1$ kpc. We note, however, that our model suggests that cosmic ray distribution is almost uniform at scales of order 10 kpc.

It cannot be excluded that the synthetic polarization maps exaggerate the relative height of the central peak because they neglect Faraday depolarization due to random magnetic fields, namely the internal Faraday dispersion discussed in Sect. 4.2. As follows from Eq. (8), and discussion following it, it is not implausible that this effect can reduce the relative height of the central peak by a factor of five or somewhat less. As can be seen from Fig. 11, the ratio of the central to the secondary peaks at a distance of about $50''$ from the centre is about 20 or more for the non-uniform distributions of cosmic rays, whereas the observed ratio is about 2–3. Given the uncertainty of any estimates of the amount of depolarization, we cannot exclude that models with a non-uniform distribution of cosmic rays could be reconciled with observations.

We show in Fig. 12 the ratio of polarized intensity observed at $\lambda 6.2$ cm to the integral along the line of sight $\int B_{\perp}^2 ds$, with B_{\perp} the component of the modelled magnetic field in the sky plane. The latter is proportional to the synthetic polarized intensity obtained for a uniform cosmic ray distribution. If our magnetic field model were perfect, the above ratio would show the variation of cosmic rays across the galactic image. We note that the value of the ratio varies remarkably little in the bar region; the most prominent variations arise from the local peaks of the observed polarized intensity that are also prominent in Fig. 9. Figure 12 confirms that the variation of cosmic ray energy density within the galaxy is rather weak and consists of a large-scale, smooth

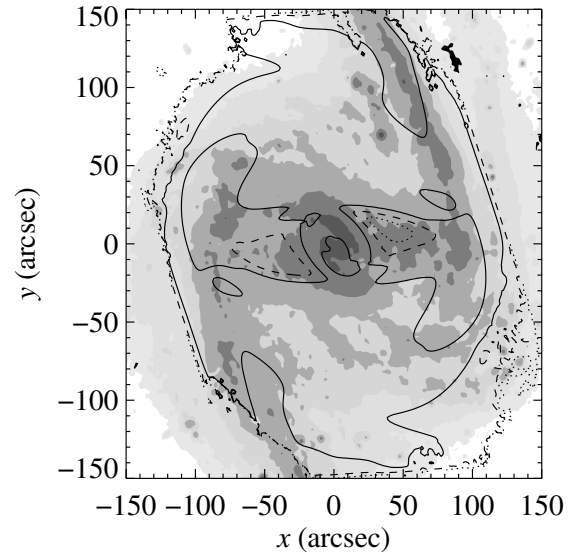


Fig. 13. The alignment of the regular magnetic and velocity fields (in the non-rotating frame) illustrated with the contours of $\cos \chi = |\mathbf{u} \cdot \mathbf{B}|/uB$ at the midplane for Model 2, projected on to the optical image in the plane of the sky. The levels shown are 0.4 (dotted), 0.7 (dashed) and 0.95 (solid).

variation with contours of a shape similar to that of gas density and other tracers in the bar, and perhaps with a few local maxima.

5.2. The effects of the turbulent magnetic diffusivity

Models 2 and 4 yield very similar magnetic field distributions (see Fig. 6), even though the background turbulent magnetic diffusivity η_0 in Model 4 is more than twice as large as in Model 2 (see Table 1). The main effect of enhanced magnetic diffusivity is to make the secondary peaks of P in Model 4 less prominent, even with $n_{\text{cr}} = \text{const}$. Model 4 could be reconciled with observations if n_{cr} were enhanced in the outer bar regions and in the spiral arms and/or reduced in the central part. Unless this is the case, and given that Model 2 agrees with observations better than Model 4, we conclude that our models support a value $\eta_0 \lesssim 10^{26} \text{ cm}^2 \text{ s}^{-1}$ in NGC 1365.

One of the effects of turbulent magnetic diffusion (and dynamo action) is to produce a misalignment between magnetic field and velocity in a shearing flow. Since the velocity shear is strong everywhere in the bar region and near the spiral arms, we expect that magnetic and velocity fields would be tightly aligned (in the corotating frame) if magnetic field were frozen into the flow (Moss et al. 2001).

The degree of alignment between the model magnetic and velocity fields in NGC 1365 is illustrated in Fig. 13, where we note that the angle between the two vectors exceeds 20° almost everywhere in the bar. The misalignment is also significant near the spiral arms.

The local enhancements of turbulent magnetic diffusivity, by a factor of 2–3, in the dust lanes and near the galactic centre introduced in Sect. 3.2 are important in our model as they allow us to avoid excessively large strength of the large-scale magnetic field produced by extreme velocity shear in those regions. As argued by Moss et al. (2001), such a local enhancement of interstellar turbulence may be associated with instabilities of the shear flow.

5.3. The role of dynamo action

Model 3 has the same parameters as Model 2, except that $R_\alpha = 0$. Thus, this model includes the same effects of rotation and velocity shear as Model 2, but without any dynamo action. In this model, the magnetic field decays on a timescale of about 0.6 Gyr, after an initial accelerated decay near the galactic centre. However, the magnetic structure in the outer parts of the galaxy is remarkably similar to that with $R_\alpha \neq 0$. We deduce that the magnetic structure we have obtained does not depend strongly on details of the poorly known α -effect, but rather is controlled by the large-scale velocity field, which is known much more reliably. The role of the α -effect is just to maintain the magnetic field against decay, which is enhanced by the strong shear typical of barred galaxies. This situation is similar to that found when modelling another barred galaxy, NGC 1097 (Moss et al. 2001).

5.4. The effect of the speed of sound

Models 2 and 6 have different values for the speed of sound (10 and 30 km s⁻¹, respectively). The higher speed of sound results in less structure in the velocity and density fields (even though we neglected to include an equivalent increase of the turbulent magnetic diffusivity by a factor of 3, which would be necessary for strict consistency). The cuts for Model 6 have relatively weaker features in the outer parts of the galaxy. This result appears less acceptable, and we deduce that 10 km s⁻¹ is a more favourable value for the speed of sound of the gas phase, to which the regular magnetic field is coupled.

5.5. Dependence on the gas ionization fraction

For $X \gtrsim 0.2$, the synthetic cuts of P show a much greater disagreement with the observed cuts than when $X = 0.1$. For example, for the cuts in Fig. 8, the effect of increasing X (and therefore increasing depolarization) is to broaden the minima in P about $\pm 50''$, and increase the ratios of the central maximum to outer maxima (at about $\pm 100''$).

When we calculate synthetic RM for values of $X \lesssim 0.01$, the range of values obtained does not match the observed range ± 600 rad m⁻². For example, at $X = 0.01$, the maximum synthetic RM is about 350 rad m⁻².

Given that a constant ionization fraction is appropriate, our models suggest that $0.01 \lesssim X \lesssim 0.2$ to be a plausible range of values.

6. Discussion and conclusions

We have constructed a three dimensional dynamo model for NGC 1365, with the rotation curve, non-circular velocities and gas density taken from a dynamical model for this particular galaxy. Thus, although we have taken a similar approach as in our earlier studies of other specific barred galaxies (IC 4214, Moss et al. 1999; NGC 1097, Moss et al. 2001), for NGC 1097 we adopted a generic dynamical model as input, whereas here we have been able to use a bespoke model. We have tried to make a much more detailed comparison between observations and model predictions than previously – but see also a recent paper by Vollmer et al. (2006).

Of course, we have been restricted to using a mean field dynamo model – for this sort of study there is really no plausible alternative currently available. Our modelling (and that of the

earlier papers, cited above) has demonstrated that when modelling galaxies with strong non-circular velocities the role of the mean field α -coefficient is primarily to offset the inevitable diffusive decay of the field, and thus allow a steady state with fields of order equipartition strength to be maintained. The major determinant of the field structure is the non-circular velocity field (Sect. 5.3 and Moss et al. 1998a, 2001), and the main features can be expected to persist for plausible field maintenance mechanisms. We must further bear in mind the other limitations of the modelling, including the restriction to the inner part of the galaxy, $r \leq 15$ kpc, which means that boundary effects may influence results near this radius.

Our main conclusions are as follows. We see no evidence for a variation in n_{cr} as strong as in B^2 . This may imply that equipartition between cosmic rays and the regular magnetic field is *not* maintained even at global scales. The discrepancy between our crude models involving the equipartition assumption and observations can be significantly reduced if Faraday depolarization due to turbulent magnetic fields is taken into account. We have discussed this result further in Sect. 5.1.

The strongest deviations of the synthetic polarized intensity from that observed occur in the bar region, just upstream of the dust lanes. The reason for the low synthetic polarized intensity is the small value of magnetic field strength there in the model. More precisely, the depth of the minima in synthetic and observed P are similar but they occur at somewhat different positions, and those in the synthetic map are broader (see Fig. 8). However, the relative heights of the maxima in P are reproduced quite successfully. In this sense, the agreement is better than might be inferred from Fig. 9. The reason for the difference is the deep and broad minimum in the gas density in those regions. We believe this to be a shortcoming of the gas dynamical model, which was fitted to incomplete CO data. In particular, CO observations of NGC 1097 (Crosthwaite 2001) do not show the minima of the density in the bar region to be as deep as in the model of NGC 1365 used here.

Rather surprisingly, the agreement between the *orientations* of the model magnetic field and the B -vectors derived from the observed polarization vectors is not as good as that between the model and synthetic PI distributions. We have discussed this in Sect. 4.5. The reason for this difference remains unclear.

Our preferred model relies on the galactic rotation curve and gas density distribution different from those suggested by Lindblad et al. (1996); the rotation curve used is that resulting from CO observations (Sofue et al. 1999). Our results are compatible with the observed distributions of polarized synchrotron intensity and the magnitude of the Faraday rotation measure for the number densities of ionized diffuse gas of order 0.16 cm⁻³ at a distance of order 5 kpc from the centre along the bar's minor axis and 0.21 cm⁻³ in the spiral arms. With the gas dynamical model used here, this corresponds to the mean ionization fraction of 0.01–0.2.

Our models confirm that magnetic field strengths in the inner bar region can be strong enough to drive mass inflow at a rate of several solar masses a year (see also Moss et al. 2000, 2001; Beck et al. 2005). Thus, in these strongly barred, strongly magnetic galaxies, it becomes necessary to include the dynamical effects of magnetic fields in order to reproduce all features of the gas flow. It follows that self-consistent magnetohydrodynamic modelling of barred galaxies is required.

Keeping in mind our dynamical model is incomplete, at least in that azimuthal structure corresponding to odd modes is omitted, our general conclusion is that mean field dynamo models are reasonably successful in modelling magnetic fields in this

barred galaxy. Moreover, such models can also provide information about both the gas dynamical modelling process and conditions in the interstellar medium (see also the models for the “normal” spiral galaxy M31 in Moss et al. 1998b). A robust conclusion is that, contrary to widely held opinions, dynamical effects of magnetic fields cannot be everywhere ignored in galaxy modelling.

Appendix A: Synthetic radio maps

Synthetic radio maps have been obtained by computing the Stokes parameters Q and U from the magnetic field obtained from the dynamo simulations. The magnetic field was rotated to the same position in the sky as the galaxy NGC 1365, and Q and U at a given wavelength were obtained by integration along the line of sight (where the z -direction here points towards an observer at infinity):

$$Q = C \int \epsilon(\mathbf{r}) \cos[2\psi(\mathbf{r})] dz,$$

$$U = C \int \epsilon(\mathbf{r}) \sin[2\psi(\mathbf{r})] dz,$$

with allowance for Faraday rotation by the thermal ionized in the local polarization angle ψ (see, for example, Sokoloff et al. 1998 and references therein for more details). Here C is a dimensional constant whose specific value is inessential here, and ϵ is the synchrotron emissivity. We assume that the synchrotron spectral index is a constant, $q = -1$, so that $\epsilon \propto n_{\text{cr}} B_{\perp}^2$. We use models of n_{cr} from Sect. 5.1.

Depolarization due to differential Faraday rotation is included as we take

$$\psi(\mathbf{r}) = \psi_0(\mathbf{r}) + C_1 \lambda^2 \int_z^{\infty} n_e(\mathbf{r}) B_{\parallel}(\mathbf{r}) dz,$$

where λ is the wavelength of the emission and $C_1 = 0.81 \text{ rad m}^{-2} \text{ cm}^3 \mu\text{G}^{-1} \text{ pc}^{-1}$ is a dimensional constant. The number density of thermal electrons n_e was obtained from the total gas number density n as given by the gas dynamical model, assuming a constant ionization degree of X . (So we take $n_e = X \rho_{\text{gas}}/m_{\text{H}}$ with m_{H} the proton mass.)

The synthetic Stokes parameters are then given by convolving the map of raw parameters with a Gaussian beam in sky plane.

Acknowledgements. We are grateful to E. Athanassoula, P. A. B. Lindblad and P. O. Lindblad for providing their gas dynamical model of NGC 1365 and for useful discussions. We thank A. Fletcher for numerous useful discussions. This work was supported by PPARC Grants PPA/G/S/2000/00528 and PPA/S/S/2000/02975A. D.M., A.S. and D.D.S. acknowledge the hospitality and financial support of the Isaac Newton Institute for Mathematical Sciences (University of Cambridge) in 2004. R.B. and D.D.S. acknowledge financial support from DFG-RFBR project 03-02-04031. D.D.S. is grateful to RFBR for financial support under grant 04-02-16094. This work was partially supported by Swiss Nationalfonds grant 200020-101766.

References

- Beck, R., Brandenburg, A., Moss, D., Shukurov, A., & Sokoloff, D. 1996, *ARA&A*, 34, 155
- Beck, R., Shoutenkov, V., Ehle, M., et al. 2002, *A&A*, 391, 83
- Beck, R., Fletcher, A., Shukurov, A., et al. 2005, *A&A*, 444, 739
- Brandenburg, A., & Subramanian, K. 2005, *Phys. Rep.*, 417, 1-4
- Burn, B. J. 1966, *MNRAS*, 133, 67
- Curran, S. J., Polatidis, A. G., Aalto, S., & Booth, R. S. 2001, *A&A*, 373, 459
- Crosthwaite, L. P. 2001, Ph.D. Thesis, Univ. of California, Los Angeles
- Englmaier, P., & Gerhard, O. 1997, *MNRAS*, 287, 57
- Lindblad, P. O. 1999, *ARA&A*, 9, 221
- Lindblad, P. A. B., Lindblad, P. O., & Athanassoula, E. 1996, *A&A*, 313, 65
- Moss, D. 1997, *MNRAS*, 289, 554
- Moss, D., Korpi, M., Rautiainen, P., & Salo, H. 1998a, *A&A*, 329, 895
- Moss, D., Shukurov, A., Sokoloff, D., Beck, R., & Berkhuijsen, E. M. 1998b, *A&A*, 335, 500
- Moss, D., Rautiainen, P., & Salo, H. 1999, *MNRAS*, 303, 125
- Moss, D., Shukurov, A., & Sokoloff, D. 2000, *A&A*, 358, 1142
- Moss, D., Shukurov, A., Sokoloff, D., Beck, R., & Fletcher, A. 2001, *A&A*, 380, 55
- Ondrechen, M. P., & van der Hulst, J. M. 1989, *ApJ*, 342, 29
- Otmianowska-Mazur, K., Elstner, D., Soida, M., & Urbanik, M. 2002, *A&A*, 384, 48
- Roberts, P. H., & Soward, A. M. 1975, *AN*, 296, 49
- Ruzmaikin, A., Shukurov, A., & Sokoloff, D. 1988, *Magnetic Fields of Galaxies* (Dordrecht: Kluwer)
- Sandqvist, Aa., Jörsäter, S., & Lindblad, P. O. 1995, *A&A*, 295, 585
- Shukurov, A. 2004, in *Mathematical Aspects of Natural Dynamos*, ed. E. Dormy, & B. Desjardins (EDP) [arXiv:astro-ph/0411739]
- Sofue, Y., Tutui, Y., Honma, M., et al. 1999, *ApJ*, 523, 136
- Soida, M., Otmianowska-Mazur, K., Chyży, K. T., & Vollmer, B. 2006, *AN*, 327, 503
- Sokoloff, D. D., & Shukurov, A. 1990, *Nature*, 347, 51
- Sokoloff, D. D., Bykov, A. A., Shukurov, A., et al. 1999, *MNRAS* (Erratum: op. cit., 303, 207, 1999), 299, 189
- Stone, J. M., & Norman, M. L. 1992, *ApJS*, 80, 791
- Vollmer, B., Soida, M., Otmianowska-Mazur, K., et al. 2006, *A&A*, 453, 883
- Widrow, L. M. 2002, *Rev. Mod. Phys.*, 74, 775